

Three-body-fragmentation dynamics of CO_2^{4+} investigated by electron collisions at an impact energy of 500 eV

Enliang Wang, Xu Shan, Zhenjie Shen, Xingyu Li, Maomao Gong, Yaguo Tang, and Xiangjun Chen*

Hefei National Laboratory for Physical Sciences at Microscale and Department of Modern Physics,

University of Science and Technology of China, Hefei, Anhui, 230026, China

and Synergetic Innovation Center of Quantum Information and Quantum Physics, University of Science and

Technology of China, Hefei, Anhui 230026, China

(Received 22 October 2015; published 23 December 2015)

Fragmentation of CO_2^{4+} induced by electron impact at the energy of 500 eV is studied using a momentum imaging spectrometer. It is found that CO_2^{4+} decays mainly through two three-body-fragmentation channels: $\text{CO}_2^{4+} \rightarrow \text{O}^+ + \text{C}^{2+} + \text{O}^+$ (121) and $\text{CO}_2^{4+} \rightarrow \text{O}^{2+} + \text{C}^+ + \text{O}^+$ (211). The fragmentation dynamics of these two channels are analyzed using Dalitz plots and Newton diagrams. In channel (121) CO_2^{4+} dissociates mainly through linear and molecular bending fragmentation, while the asynchronous breakup mechanism dominates channel (211). The distributions of momentum correlation angles between ionic fragments and the kinetic energy releases are obtained. Based on the Coulomb explosion model, the bond angle and the bond length of CO_2^{4+} before fragmentation are reconstructed. The experimental most probable values of the O-C-O bond angle are 172° and 171° for channel (121) and (211), which agree quite well with that of the neutral CO_2 molecule (172.5°). The reconstructed values of C-O bond length, 1.20 Å and 1.13 Å from channel (121) and channel (211), are also inconsistent with the equilibrium value of the neutral CO_2 molecule (1.16 Å).

DOI: [10.1103/PhysRevA.92.062713](https://doi.org/10.1103/PhysRevA.92.062713)

PACS number(s): 34.80.Gs, 34.50.Gb

I. INTRODUCTION

Fragmentation dynamics of multicharged polyatomic molecules has captured continuous interests [1–5] in the past two decades and has been investigated in detail by experiments using highly charged ions (HCIs) [6,7], electrons [8–11], synchrotron radiation [12–16], and intense laser fields [3,17–20]. Early experiments usually employed time-of-flight (TOF) systems to detect the ionic fragments. Different dissociative channels can be distinguished by analyzing the TOF correlations between ion pairs [21,22], and the kinetic energy release (KER) for each channel can be deduced [23]. However, only the projection of the momentum vector along the axis of the TOF system can be reconstructed. In recent years, with the rapidly developing ion momentum imaging techniques [24,25], it is now possible to detect all the charged fragments in coincidence. By placing the position-sensitive detector (PSD) [26] at the end of the TOF system, both the positions and TOF of the detected ionic fragments can be measured. This enables one to reconstruct the three-dimensional momentum vectors. By analyzing the momentum correlations between fragments, the mechanism of molecular bond breakage can be clarified [7,11,27]. Furthermore, with the help of the commonly adopted Coulomb explosion (CE) model [28,29], the kinematically complete measurement of the momentum vectors of all the fragments provides a way to image the molecular geometry at the instant of the fragmentation.

Carbon dioxide, which plays an essential role in planetary atmosphere and interstellar space, is a prototype sample for exploring fragmentation dynamics of small molecules [7,11,27]. The fragmentation dynamics of CO_2 has been extensively investigated by using synchrotron radiation [30], electrons [11,31,32], HCIs [7,33–35] as well as intense laser

field [20,27,36–39]. Up to now, the breakup mechanism as well as the momentum correlation angle (MCA) and KER distributions for CO_2^{q+} ($q \leq 3$) have been investigated in detail. It was demonstrated that, for the lowly charged CO_2 , the chemical bonds do not always break up through the nonsequential process, i.e., the bonds break up through the one-step process. The fragmentation can occur in a sequential way by breaking bonds step by step [7,11,27,32]. Recently, it was also found that the intermediate electronic states of the CO_2 ion play an important role in the fragmentation dynamics [11]. However, the studies of three-body fragmentation of highly charged CO_2^{q+} ($q \geq 4$) are quite scarce. Siegmann *et al.* studied the fragmentation of CO_2^{q+} ($q = 3–6$) in collisions with 5.9 MeV/u Xe^{18+} and Xe^{43+} ions [40]. They found that, based on the CE model, the reconstructed O-C-O bond angle was in reasonable agreement with that of neutral CO_2 which deviates from the linear configuration due to the noticeable population of higher vibration levels of the bending modes at room temperature. But the CE model is insufficient to explain the observed KER distributions. The three-body fragmentation of CO_2^{q+} ($q = 3 \sim 6$) in an intense laser field was investigated systematically using the triple coincidence imaging technique [36,39,41]. The KERs obtained in the intense laser field experiments are always considerably lower than would be expected from the CE picture employing the equilibrium geometry of the neutral molecule. The reconstructed bond lengths from the CE model are channel dependent and usually are 2–3 times the equilibrium bond lengths [39,41]. This is due to the substantial deformation of the molecular structure in the laser field [36] and can be described by either the classical enhanced ionization model [39] or the quantum charge resonance enhanced ionization model [41].

As for electron collision experiment, only partial ionization cross sections (PICSSs) of CO_2^{4+} have been measured [42]. This is because the cross section for forming the multicharged molecular ion is extremely small [42]. In the present work, the

*xjun@ustc.edu.cn

fragmentation dynamics of quadruply ionized CO_2 formed by electron collision at 500 eV is studied using an ion momentum imaging spectrometer [43]. By using the newly developed high efficiency coincidence technique [44], the three ionic fragments are detected in coincidence in the experiment. The momentum vector of each charged fragment is measured and the MCA distributions as well as the KER distributions are obtained. By analyzing Dalitz plots and Newton diagrams, the fragmentation mechanism of each dissociative channel is studied. Based on the CE model, the bond angle and the bond length of CO_2^{4+} before fragmentation are also determined.

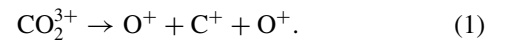
II. EXPERIMENT

The experiment is carried out using an electron impact ion momentum imaging spectrometer, which was built up recently in our laboratory [43–45]. The working principle is similar to the reaction microscope [24,25]. Briefly, a pulsed electron beam from a thermal cathode electron gun is injected into the reaction center to collide with the gas-phase molecules effusing from a capillary which is mounted on a manipulator, with the help of which the capillary is adjusted to the position of the ground potential of the extraction field to eliminate field distortions. The inner and outer diameters and length of the capillary are 0.1, 0.3, and 50 mm, respectively. After the collision, a pulsed extraction field (50 V/cm) is applied to extract the ions. A TOF mass spectrometer is employed to detect the ions with 4π solid angle collection efficiency. The lengths of the acceleration and the field-free drift region are 50 and 100 mm, respectively. At the end of the TOF system, a multihit time- and position-sensitive detector is used to detect the TOF and hit positions of the ions. In this work, a high efficiency multicoincidence technique [44] is used to measure the three charged fragments in coincidence. In the experiment, the pulse width and repetition frequency of the electron beam are 10 ns and 15 kHz, respectively. The equivalent beam current is about 15 pA. The background vacuum is better than 5.0×10^{-6} Pa and the working pressure is 1.0×10^{-4} Pa. The triple coincidence count rate is about 20 Hz which is far less than the electron beam repetition frequency ensuring a high

signal to background ratio. The signal of the pulsed electron gun is used as the trigger of the data acquisition system and the multihit time and position signals of ions are recorded by a multihit time-to-digital converter. The momentum vector of each ion is obtained by the observed TOF, t , and position (x, y) .

III. RESULTS AND DISCUSSION

The quadruply ionized molecular ion CO_2^{4+} is formed by electron impact multiple ionization of CO_2 . Under present impact energy $E_e = 500$ eV, it is unlikely that the four electrons are ejected in a direct mechanism, i.e., $(e, 5e)$ process. As revealed by the works of synchrotron radiation-induced multiple Auger decay of Ne [46], OCS [47], and CO_2 [16], the most probable way to create CO_2^{4+} is carbon K -shell ionization followed by multiple Auger decay. In this case, the timing scale for creating CO_2^{4+} is about several femtoseconds. The ion-ion coincidence spectra are shown in Fig. 1, in which the correlations of the TOF of the first hit ion versus the second one and the TOF of the first hit ion versus the third one are depicted in Figs. 1(a) and 1(b), respectively. The dissociative channels can be identified and separated using these coincidence spectra. For a certain dissociative channel, the true events will distribute along an island on the coincidence spectra due to the momentum correlation. The two-body or three-body dissociative channels of CO_2^{2+} , for which only two charged fragments will be formed, can be identified only using the coincidence of the first and second hit ions. For three-body dissociative channels of CO_2^{3+} or CO_2^{4+} , however, there will be three produced charged fragments that must be detected in triple coincidence. In order to identify these channels, the triple coincidence method, which has been described in detail in Ref. [43], is introduced in the data analyzing process. Briefly, the coincidence of $\text{C}^+ + \text{O}^+$ in Figs. 1(a) and 1(b) determine the three-body dissociative channel of CO_2^{3+} (111),



The coincidence of $\text{C}^{2+} + \text{O}^+$ in Fig. 1(a) and the coincidence of $\text{C}^{2+} + \text{O}^+$ in Fig. 1(b) determine the dissociative channel

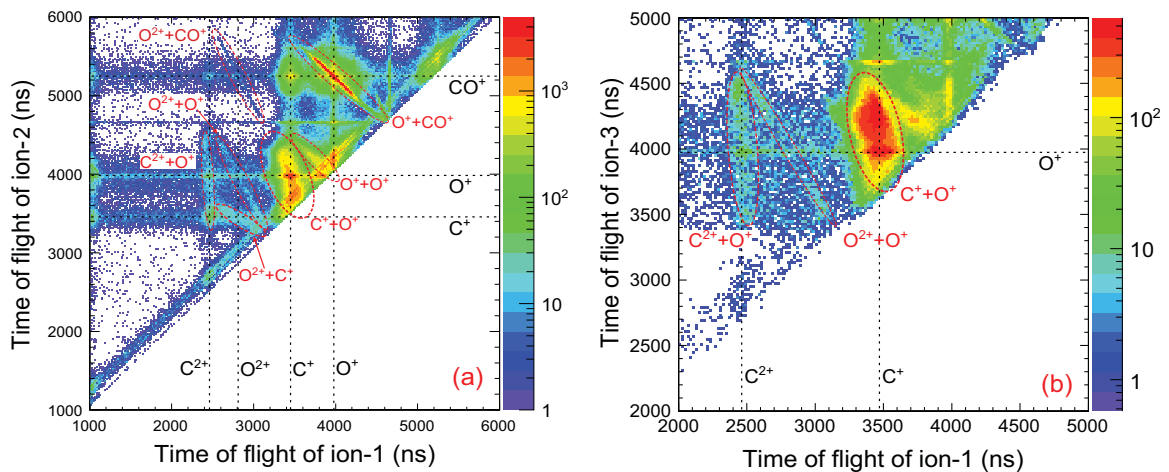
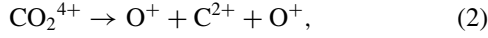
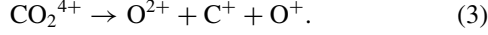


FIG. 1. (Color online) Ion-ion coincidence spectra for identifying different dissociative channels. (a) Correlation spectra of time of flight of the first hit ion versus the second one. (b) Correlation spectra of time of flight of the first hit ion versus the third one.

(121),



while the coincidence of $\text{O}^{2+} + \text{C}^+$ in Fig. 1(a) and the coincidence of $\text{O}^{2+} + \text{O}^+$ in Fig. 1(b) determine the dissociative channel (211),



In the data analyzing process, the three-body dissociative events are first selected by triple coincidence method and are further selected using the momentum conservation condition [48], which ensures that the three ions originate from the same molecular ion. The relative intensities of channel (111), (121), and (211) are 72.5 : 1.3 : 1.

A. Momentum correlations and angular distributions

In order to analyze the dissociative mechanism we employ the Dalitz plot [49] in which the Cartesian coordinates of each point are obtained by the normalized kinetic energies of the three fragments,

$$x = \frac{\varepsilon_1 - \varepsilon_3}{\sqrt{3}\varepsilon_k}, \quad (4)$$

$$y = \frac{\varepsilon_2}{\varepsilon_k} - \frac{1}{3}, \quad (5)$$

where ε_i is the kinetic energy of the i th fragment [$i = 1, 2, 3$ for O^+ , C^{2+} , and O^+ of channel (121) and for O^{2+} , C^+ , and O^+ of channel (211)]; $\varepsilon_k = \varepsilon_1 + \varepsilon_2 + \varepsilon_3$ is the total kinetic energy. In the Dalitz plot, each point represents a specific momentum correlation among the three fragments [7,11]. The experimental Dalitz plots of channels (121) and (211) are shown in Figs. 2(a) and 2(b), respectively. For channel (121), the most intense area locates near $(0, -1/3)$ indicating that the linear fragmentation dominates in this channel. There are also some data located along the y axis indicating that CO_2^{4+} has some possibility to dissociate through molecular bending fragmentation. Different from channel (121), as shown in

Fig. 2(b), most of the events locate at the bottom right of the Dalitz plot for channel (211) indicating the asynchronous breakup mechanism predominates in this channel. In this case, the two bonds of CO_2^{4+} break simultaneously, at the moment of which the C^+-O^{2+} bond stretches more than the C^+-O^+ bond. In a very recent work of Khan *et al.* [35] by HClIs, they found that for channel (211) the sequential fragmentation only occurs via $\text{O}^{2+} + \text{CO}^+$. Here, we also see some events scattered along a weak linear trace at the right side of the plot, but this cannot be confirmed due to the very low statistics.

The fragmentation mechanism can be depicted more directly with the help of the Newton diagram [7,11,27]. In the Newton diagram the momentum vector of the O^+ ion is fixed along the x axis while the momenta of the C ion and another O ion are located in the upper and lower half of the plot, respectively. The momentum magnitudes of all the three ions are normalized to the momentum magnitude of the O ion that is located in the x axis. The Newton diagram of channel (121) is shown in Fig. 3(a). In this case, the two O^+ ions are indistinguishable and they share equivalent momentum. As a result, the island of O^+ in the lower half plane of the Newton diagram is scattered on an arc with unit radius. The island of C^{2+} of channel (121) is located near the origin of the Newton diagram indicating that most of the C^{2+} ions are emitted with almost zero momenta. The Newton diagram of channel (211) is shown in Fig. 3(c). In this case, the momentum shared by O^{2+} is larger than that of O^+ . This is clearly shown in the Newton diagram that the distance from the origin to the most intense point of the island of O^{2+} is larger than one unit.

The distribution of the islands in the Newton diagram can be reflected by the MCA distributions between the corresponding ions. The MCA can be obtained by the momentum vectors (\vec{p}_1, \vec{p}_2) of the two associated ions,

$$\alpha = \cos^{-1} \left(\frac{\vec{p}_1 \cdot \vec{p}_2}{|\vec{p}_1| |\vec{p}_2|} \right). \quad (6)$$

The MCA distributions of channel (121) are shown in Fig. 3(b). The MCA between C^{2+} and one of the O^+ ions (θ) ranges from about 60° to 120° with the most probable value of about 97° .

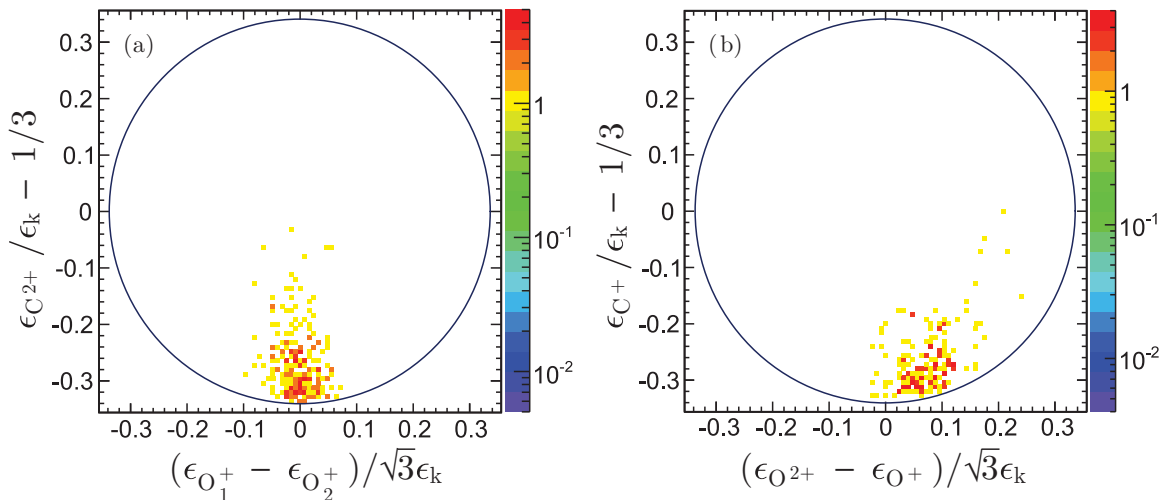


FIG. 2. (Color online) Experimental Dalitz plots of three-body fragmentation of CO_2^{4+} , (a) for $\text{CO}_2^{4+} \rightarrow \text{O}^+ + \text{C}^{2+} + \text{O}^+$ and (b) for $\text{CO}_2^{4+} \rightarrow \text{O}^{2+} + \text{C}^+ + \text{O}^+$.

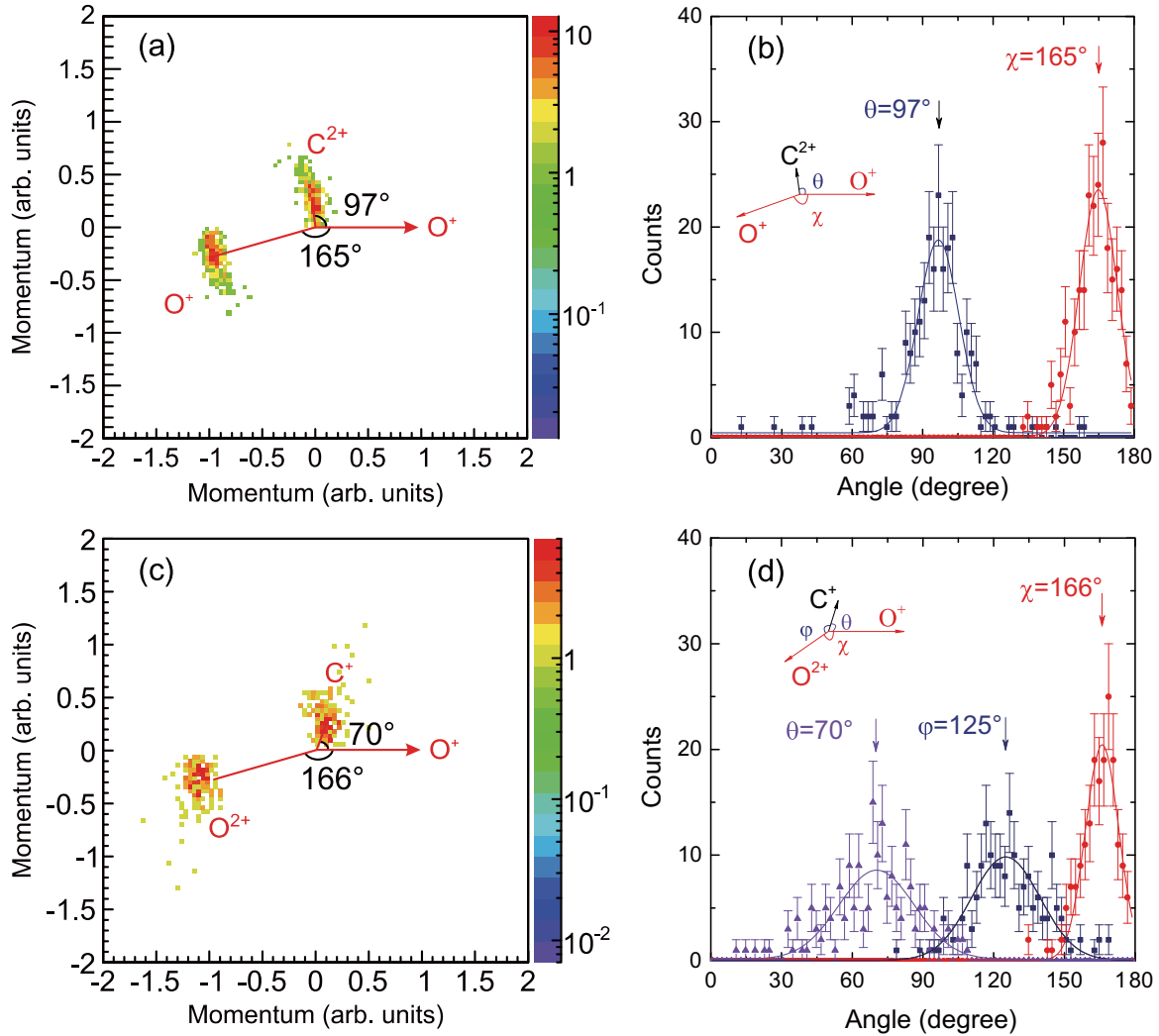


FIG. 3. (Color online) Newton diagrams and momentum correlation angle (MCA) distributions of three-body fragmentation of CO_2^{4+} . (a) Newton diagram and (b) MCA distributions of $\text{CO}_2^{4+} \rightarrow \text{O}^+ + \text{C}^{2+} + \text{O}^+$. (c) Newton diagram and (d) MCA distributions of $\text{CO}_2^{4+} \rightarrow \text{O}^{2+} + \text{C}^+ + \text{O}^+$. The solid lines in (b) and (d) are Gaussian fitted curves.

The range of MCA between two O^+ s (χ) is from less than 150° to 180° with the most probable value of about 165° . For channel (211), the MCA between C^+ and O^{2+} (φ) is larger than that between C^+ and O^+ (θ). As shown in Fig. 3(d), the most probable value of the angular distributions of φ and θ are 125° and 70° , respectively. This feature can be explained by the CE model where the Coulomb repulsion between C^+ and O^{2+} is much larger than that between C^+ and O^+ . The most probable value of the MCA distribution between two O ions (χ) of channel (211) is about 166° .

The molecular bond angle before fragmentation can be reconstructed from MCA based on the CE model. Generally, there is no analytical relationship between the molecular bond angle γ and MCA χ , as shown in the inset of Fig. 4(a). The relationship between the initial molecular geometry and the final momentum vectors of the fragments can be determined by theoretical simulation [20,50]. In order to obtain the bond angle, a numerical simulation of the explosion dynamics of CO_2^{4+} is performed by assuming the fragmentation ions moving in a Coulomb repulsive potential. In the simulation,

the bond lengths of the two C-O bonds, which are set equal to each other before fragmentation, and the bond angle are regarded as independent variables. The dependence of MCA χ as functions of the O-C-O bond angle γ and the C-O bond length for channels (121) and (211) are shown in Figs. 4(a) and 4(b), respectively. Similar to the result of Wu *et al.* [20], the variation of bond length almost has no effect on the relationship between angle χ and γ . Therefore, the relationships between angle χ and γ at bond length of $R_{\text{CO}} = 1.16 \text{ \AA}$, as shown in Fig. 4(c) for channel (121) and in Fig. 4(d) for channel (211), are adopted to reconstruct the molecular bond angles. The experimental O-C-O bond angle distributions for channel (121) and channel (211) are shown in Figs. 4(e) and 4(f), respectively. The distributions for the two channels are similar to each other, both ranging from about 150° to 180° with most probable values at 172° and 171° , respectively. The results are precisely inconsistent with the Monte Carlo simulation by Siegmann *et al.* [40]. In their simulation, by considering the population of higher vibration levels of the bending modes of CO_2 at room temperature, the obtained O-C-O bond angle

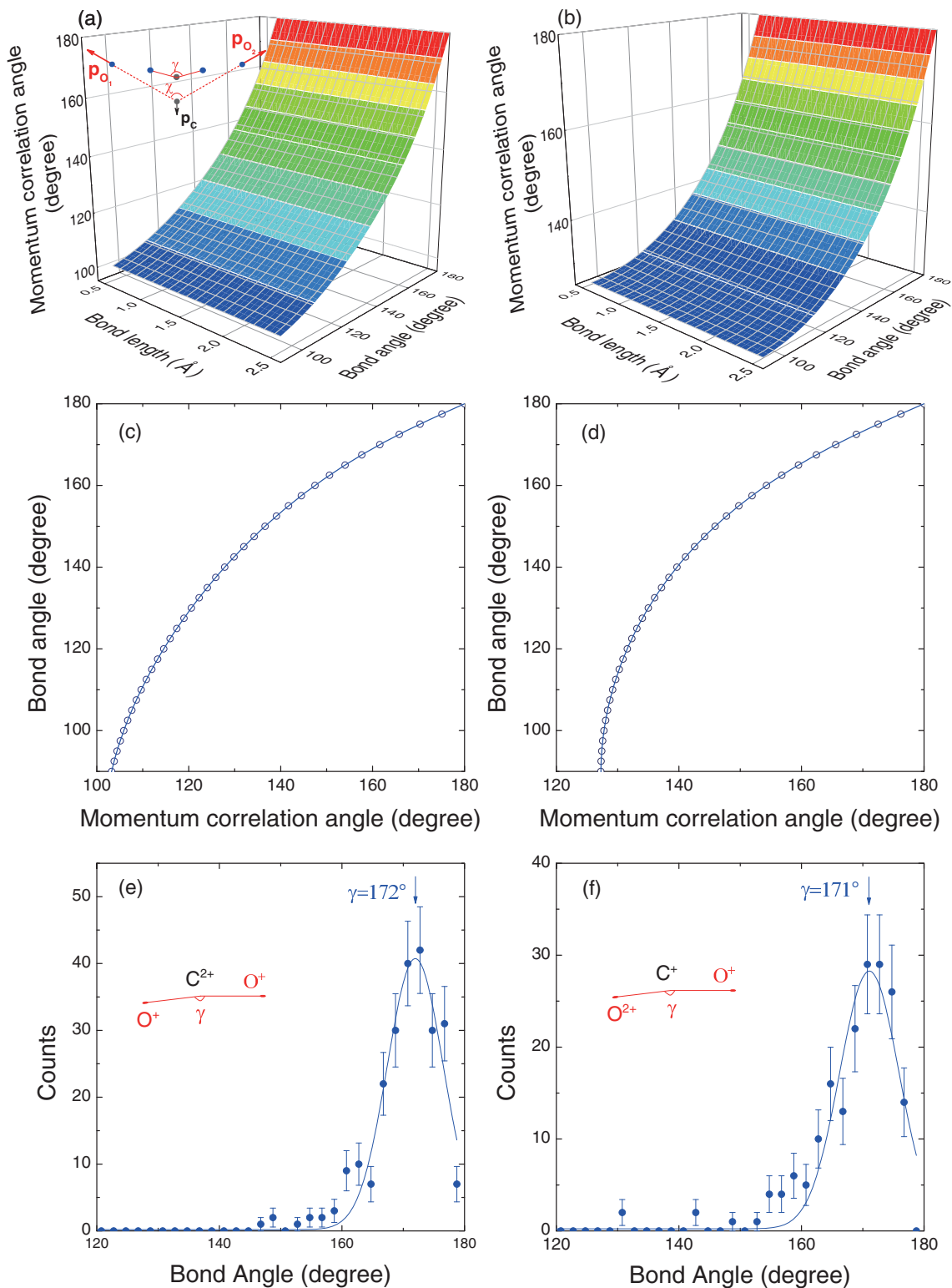


FIG. 4. (Color online) Theoretical simulations of the relationship between the momentum correlation angle χ , O-C-O bond angle γ , and the C-O bond length of (a) channel (121) and (b) channel (211). The relationships between momentum correlation angle χ and O-C-O bond angle γ at bond length of $R_{CO} = 1.16$ Å of (c) channel (121) and (d) channel (211). The experimental O-C-O bond angle distributions of (e) channel (121) and (f) channel (211).

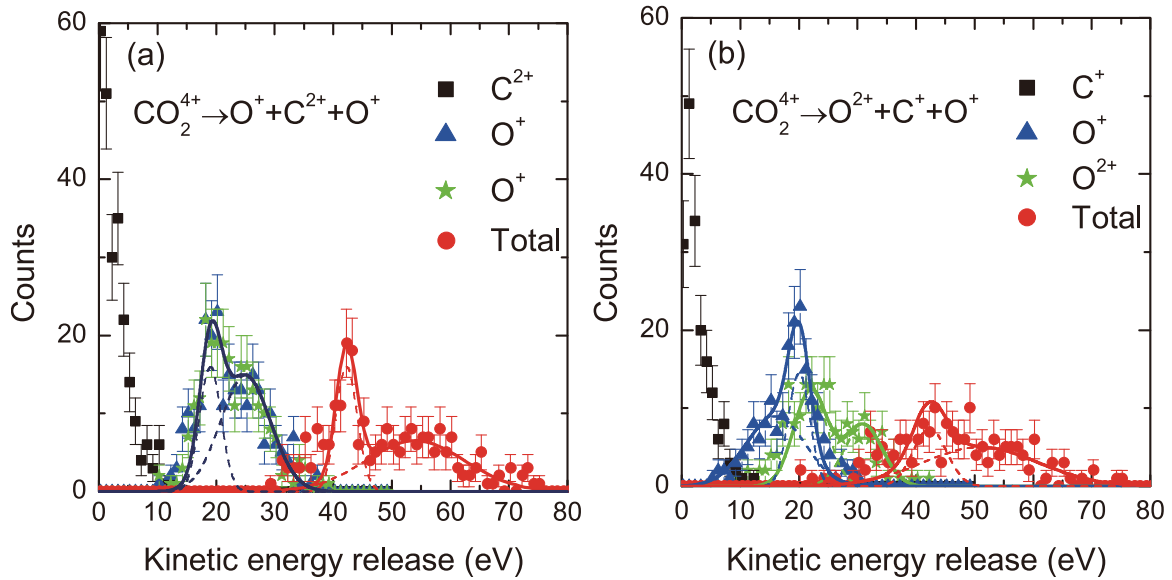


FIG. 5. (Color online) The KER distributions of three fragmentations as well as the total KER distribution for (a) $\text{CO}_2^{4+} \rightarrow \text{O}^+ + \text{C}^{2+} + \text{O}^+$ and (b) $\text{CO}_2^{4+} \rightarrow \text{O}^{2+} + \text{C}^+ + \text{O}^+$.

distribution ranges from 150° to 180° with the most probable value of 172.5° .

B. Kinetic energy releases

The KER distributions of the three fragment ions as well as the total KER distributions for channels (121) and (211) are shown in Figs. 5(a) and 5(b), respectively. The KER distributions for C ions for the two channels are both located near the origin. The peak value of KER distribution for the C ion of channel (121) is zero ($E_C = 0$), while that of channel (211) is slightly larger than 0 ($E_C > 0$), which is due to the larger Coulomb repulsive force between O^{2+} and C^+ resulting in the C^+ moving toward O^+ in channel (211).

The total KER distributions as well as KER distributions of O ions obtained in this work are quite different from the previous works by HCIs [40] or intense laser field [39]. In the work of Siegmann *et al.* by HCIs, a broad no-structured total KER distribution extended from 25 to 100 eV with a peak value at ~ 57 eV for channel (121) was observed. Two identical KER distributions for the two O^+ were also observed with peak value at ~ 27 eV. The peak values for total and O^+ KER distributions can be reproduced well by the CE model. For channel (211), the total KER showed a broader distribution with peak value at ~ 62 eV, while KER distributions of O^+ and O^{2+} exhibited different peak values at ~ 27 eV and ~ 33 eV; both are larger than the predicted values by the CE model. In the intense laser field experiments [39], on the other hand, only the total KER distributions were obtained with peak values at ~ 14 eV for channel (121) and ~ 27 eV for channel (211), much lower than HCI results as well as CE model predictions.

In the present work, distinct structures can be observed in both total and O ion KER distributions. For channel (121), the total KER shows a broad distribution from 30 to 80 eV with a sharp peak at ~ 42.5 eV overlapped on a wide lobe. Two Gaussian functions are used to fit the peak and the

lobe. The peak value of the lobe is about 54 eV, which is to coincide with the KER (~ 56 eV) estimated by the CE model. Correspondingly, two structures are also observed in the two identical KER distributions of the two O^+ s, a narrow peak at ~ 19 eV and a wider one at ~ 25 eV as indicated by two fitted Gaussian functions. Apparently, the wider peak at ~ 25 eV is attributed to the CE, in which two O^+ ions share the total KER while leaving the C^{2+} ion almost at rest. The narrow peak, on the other hand, corresponds to the sharp peak at ~ 42.5 eV in total KER distribution. This sharp peak can only be ascribed to a weak bonding low energy state of CO_2^{4+} .

For channel (211), the total KER also shows a broad distribution from 20 to 80 eV with a weak peak at ~ 43 eV. Here again, two Gaussian functions are invoked to fit the peak and the wide lobe. The most probable value of the lobe structure is ~ 51 eV, inconsistent with the value (~ 50 eV) evaluated by the CE model. The total KER will be shared mainly by the two O ions. The KER of O^{2+} is basically larger than that of O^+ , which is due to the larger Coulomb repulsive force between C^+ and O^{2+} than that between C^+ and O^+ . For O^{2+} , two peaks are observed at ~ 22 eV and ~ 31 eV, while a peak at ~ 20 eV and a shoulder at ~ 16 eV are observed for KER distribution of O^+ .

Based on the CE model, the bond length of CO_2^{4+} before fragmentation can also be deduced from the KER distributions. Here, the Gaussian fitted peak values of the wide lobes of the total KER distributions are adopted to do the reconstruction. The C-O bond lengths reconstructed from the experimental data of channels (121) and (211) are $R_{\text{CO}} = 1.20 \text{ \AA}$ and $R_{\text{CO}} = 1.13 \text{ \AA}$, which both agree well with the bond length of the neutral CO_2 molecule ($R_{\text{CO}} = 1.16 \text{ \AA}$).

IV. SUMMARY

The three-body-fragmentation dynamics of CO_2^{4+} is investigated by electron collision at impact energy of 500 eV using a momentum imaging spectrometer. Two dissociative

channels, $\text{CO}_2^{4+} \rightarrow \text{O}^+ + \text{C}^{2+} + \text{O}^+$ (121) and $\text{CO}_2^{4+} \rightarrow \text{O}^{2+} + \text{C}^+ + \text{O}^+$ (211), dominate the fragmentation of CO_2^{4+} . The correlations among all the fragments of each channel are analyzed using Dalitz plots as well as Newton diagrams. It is found that channel (121) dissociates mainly through linear and molecular bending fragmentation where the two O^+ s are emitted symmetrically and the asymmetry breakup mechanism dominates in channel (211) where O^{2+} shares more momentum than that of O^+ . The molecular bond angle distributions before fragmentation are reconstructed from MCA distributions based on the CE model. The experimental most probable values of the O-C-O bond angle are 172° and 171° for channels (121) and (211), which agree quite well with that of the neutral CO_2

molecule (172.5°). The reconstructed values of the C-O bond length from the KER data are also inconsistent with the value of the neutral CO_2 molecule.

ACKNOWLEDGMENTS

This work was jointly supported by the National Natural Science Foundation of China (Grants No. 11534011, No. 11327404, No. 11404317, and No. U1432118), the Scientific Research Grant of Hefei Science Center of CAS (Grant No. 2015SRG-HSC039), and the Fundamental Research Funds for the Central Universities and China Postdoctoral Science Foundation (Grant No. 2014M561824).

-
- [1] D. Mathur, *Phys. Rep.* **225**, 193 (1993).
 [2] D. Mathur, *Phys. Rep.* **391**, 1 (2004).
 [3] J. H. Posthumus, *Rep. Prog. Phys.* **67**, 623 (2004).
 [4] J. Ullrich, A. Rudenko, and R. Moshhammer, *Annu. Rev. Phys. Chem.* **63**, 635 (2012).
 [5] J. Ullrich and V. P. Shevel, *Many-Particle Quantum Dynamics in Atomic and Molecular Fragmentation* (Springer, New York, 2003).
 [6] L. Adoui, M. Tarisien, J. Rangama, P. Sobocinsky, A. Cassimi, J.-Y. Chesnel, F. Frémont, B. Gervais, A. Dubois, M. Krishnamurthy, Sanjay Kumar, and D. Mathur, *Phys. Scr.* **T92**, 89 (2001).
 [7] N. Neumann, D. Hant, L. Ph. H. Schmidt, J. Titze, T. Jahnke, A. Czasch, M. S. Schöffler, K. Kreidi, O. Jagutzki, H. Schmidt-Böcking, and R. Dörner, *Phys. Rev. Lett.* **104**, 103201 (2010).
 [8] R. Singh, P. Bhatt, N. Yadav, and R. Shanker, *Phys. Rev. A* **87**, 022709 (2013).
 [9] X. Ren, T. Pflüger, M. Weyland, W. Y. Baek, H. Rabus, J. Ullrich, and A. Dorn, *J. Chem. Phys.* **141**, 134314 (2014).
 [10] T. Pflüger, X. Ren, and A. Dorn, *Phys. Rev. A* **91**, 052701 (2015).
 [11] E. Wang, X. Shan, Z. Shen, M. Gong, Y. Tang, Y. Pan, K.-C. Lau, and X. Chen, *Phys. Rev. A* **91**, 052711 (2015).
 [12] T. Masuoka and I. Koyano, *J. Chem. Phys.* **95**, 909 (1991).
 [13] H. Shizuka and H. D. E. John, *J. Phys. B* **30**, 4515 (1997).
 [14] U. Becker, *J. Electron Spectrosc. Relat. Phenom.* **96**, 105 (1998).
 [15] T. Weber, O. Jagutzki, M. Hattass, A. Staudte, A. Nauert, L. Schmidt, M. H. Prior, A. L. Landers, A. Bräuning-Demian, H. Bräuning, C. L. Cocke, T. Osipov, I. Ali, R. Díez Muiño, D. Rolles, F. J. García de Abajo, C. S. Fadley, M. A. Van Hove, A. Cassimi, H. Schmidt-Böcking, and R. Dörner, *J. Phys. B* **34**, 3669 (2001).
 [16] J. H. D. Eland, L. Andric, P. Linusson, L. Hedin, S. Plogmaker, J. Palaudoux, F. Penent, P. Lablanquie, and R. Feifel, *J. Chem. Phys.* **135**, 134309 (2011).
 [17] B. Wales, É. Bisson, R. Karimi, S. Beaulieu, A. Ramadhan, M. Giguère, Z. Long, W.-K. Liu, J.-C. Kieffer, F. Légaré, and J. Sanderson, *J. Electron Spectrosc. Relat. Phenom.* **195**, 332 (2014).
 [18] C. Wu, C. Wu, D. Song, H. Su, X. Xie, M. Li, Y. Deng, Y. Liu, and Q. Gong, *J. Chem. Phys.* **140**, 141101 (2014).
 [19] A. Hishikawa and K. Yamanouchi, in *Progress in Ultrafast Intense Laser Science II* (Springer, Berlin, Heidelberg, 2007), Chap. 1.
 [20] C. Wu, C. Wu, Y. Fan, X. Xie, P. Wang, Y. Deng, Y. Liu, and Q. Gong, *J. Chem. Phys.* **142**, 124303 (2015).
 [21] L. J. Frainski, K. Codling, and P. A. Hatherly, *Science* **246**, 1029 (1989).
 [22] J. H. D. Eland, *Mol. Phys.* **61**, 725 (1987).
 [23] G. Dujardin and D. Winkoun, *J. Chem. Phys.* **83**, 6222 (1985).
 [24] R. Dörner, V. Mergel, O. Jagutzki, L. Spielberger, J. Ullrich, R. Moshhammer, and H. Schmidt-Böcking, *Phys. Rep.* **330**, 95 (2000).
 [25] J. Ullrich, R. Moshhammer, A. Dorn, R. Dörner, L. Ph. H. Schmidt, and H. Schmidt-Böcking, *Rep. Prog. Phys.* **66**, 1463 (2003).
 [26] S. E. Sobottka and M. B. Williams, *IEEE Trans. Nucl. Sci.* **35**, 348 (1988).
 [27] C. Wu, C. Wu, D. Song, H. Su, Y. Yang, Z. Wu, X. Liu, H. Liu, M. Li, Y. Deng, Y. Liu, L.-Y. Peng, H. Jiang, and Q. Gong, *Phys. Rev. Lett.* **110**, 103601 (2013).
 [28] Z. Vager, R. Naaman, and E. P. Kanter, *Science* **244**, 426 (1989).
 [29] M. Pitzer, M. Kunitski, A. S. Johnson, T. Jahnke, H. Sann, F. Sturm, L. Ph. H. Schmidt, H. Schmidt-Böcking, R. Dörner, J. Stohner, J. Kiedrowski, M. Reggelin, S. Marquardt, A. Schießler, R. Berger, and M. S. Schöffler, *Science* **341**, 1096 (2013).
 [30] R. K. Singh, G. S. Lodha, V. Sharma, I. A. Prajapati, K. P. Subramanian, and B. Bapat, *Phys. Rev. A* **74**, 022708 (2006).
 [31] P. Bhatt, R. Singh, N. Yadav, and R. Shanker, *Phys. Rev. A* **85**, 042707 (2012).
 [32] X. Wang, Y. Zhang, D. Lu, G. C. Lu, B. Wei, B. H. Zhang, Y. J. Tang, R. Hutton, and Y. Zou, *Phys. Rev. A* **90**, 062705 (2014).
 [33] L. Adoui, T. Muranaka, M. Tarisien, S. Legendre, G. Laurent, A. Cassimi, J.-Y. Chesnel, X. Fléhard, F. Frémont, B. Gervais, E. Giglio, and D. Hennecart, *Nucl. Instrum. Methods B* **245**, 94 (2006).
 [34] M. R. Jana, P. N. Ghosh, B. Bapat, R. K. Kushawaha, K. Saha, I. A. Prajapati, and C. P. Safvan, *Phys. Rev. A* **84**, 062715 (2011).
 [35] A. Khan, L. C. Tribedi, and D. Misra, *Phys. Rev. A* **92**, 030701(R) (2015).
 [36] A. Hishikawa, A. Iwamae, and K. Yamanouchi, *Phys. Rev. Lett.* **83**, 1127 (1999).
 [37] K. Zhao, G. Zhang, and W. T. Hill, *Phys. Rev. A* **68**, 063408 (2003).
 [38] S. Minemoto, T. Kanai, and H. Sakai, *Phys. Rev. A* **77**, 041401 (2008).

- [39] J. P. Brichta, S. J. Walker, R. Helsten, and J. H. Sanderson, *J. Phys. B* **40**, 117 (2007).
- [40] B. Siegmann, U. Werner, H. O. Lutz, and R. Mann, *J. Phys. B* **35**, 3755 (2002).
- [41] I. Bocharova, R. Karimi, E. F. Penka, J.-P. Brichta, P. Lassonde, X. Fu, J.-C. Kieffer, A. D. Bandrauk, I. Litvinyuk, J. Sanderson, and F. Légaré, *Phys. Rev. Lett.* **107**, 063201 (2011).
- [42] C. Tian and C. R. Vidal, *Phys. Rev. A* **58**, 3783 (1998).
- [43] E. Wang, X. Shan, Y. Shi, Y. Tang, and X. Chen, *Rev. Sci. Instrum.* **84**, 123110 (2013).
- [44] E. Wang, Y. Tang, Z. Shen, M. Gong, X. Shan, and X. Chen, *Rev. Sci. Instrum.* **86**, 066108 (2015).
- [45] E.-L. Wang, Z.-J. Shen, H.-J. Yang, Y.-G. Tang, X. Shan, and X.-J. Chen, *Chin. Phys. B* **23**, 113404 (2014).
- [46] Y. Hikosaka, T. Kaneyasu, P. Lablanquie, F. Penent, E. Shigemasa, and K. Ito, *Phys. Rev. A* **92**, 033413 (2015).
- [47] J. H. D. Eland, M. Hochlaf, P. Linusson, E. Andersson, L. Hedin, and R. Feifel, *J. Chem. Phys.* **132**, 014311 (2010).
- [48] A. Matsuda, E. J. Takahashi, and A. Hishikawa, *J. Chem. Phys.* **127**, 114318 (2007).
- [49] R. H. Dalitz, *Philos. Mag.* **44**, 1068 (1953).
- [50] M. Kunitski, S. Zeller, J. Voigtsberger, A. Kalinin, L. Ph. H. Schmidt, M. Schöffler, A. Czasch, W. Schöllkopf, R. E. Grisenti, T. Jahnke, D. Blume, and R. Dörner, *Science* **348**, 551 (2015).